

Polariton hyperspectral imaging of two-dimensional semiconductor crystals

Christian Gebhardt,^{1,2} Michael Förg,³ Hisato Yamaguchi,⁴ Ismail Bilgin,⁴ Aditya D. Mohite,⁴ Christopher Gies,⁵ Malte Hartmann,⁵ Matthias Florian,⁵ Theodor W. Hänsch,^{1,2} Alexander Högele,³ and David Hunger^{6,*}

¹*Fakultät für Physik, Ludwig-Maximilians-Universität, Schellingstraße 4, 80799 München, Germany*

²*Max-Planck-Institut für Quantenoptik, Hans-Kopfermann-Str. 1, 85748 Garching, Germany*

³*Fakultät für Physik, Munich Quantum Center, and Center for NanoScience (CeNS),*

Ludwig-Maximilians-Universität, Geschwister-Scholl-Platz 1, 80539 München, Germany

⁴*3MPA-11 Materials Synthesis and Integrated Devices, Materials Physics and Applications Division, Los Alamos National Laboratory (LANL), Los Alamos, New Mexico 87545, USA*

⁵*Institut für Theoretische Physik, Universität Bremen, 28334 Bremen, Germany*

⁶*Physikalisches Institut, Karlsruher Institut für Technologie, Wolfgang-Gaede-Str.1, 76131 Karlsruhe, Germany*

(Dated: March 26, 2018)

Atomically thin crystals of transition metal dichalcogenides (TMDs) host excitons with strong binding energies and sizable light-matter interactions. Coupled to optical cavities, monolayer TMDs routinely reach the regime of strong light-matter coupling, where excitons and photons admix coherently to form quasiparticles known as polaritons up to room temperature. Here, we explore the two-dimensional nature of TMD polaritons with cavity-assisted hyperspectral imaging. Using extended WS₂ monolayers, we establish the regime of strong coupling with a scanning microcavity to map out polariton properties and correlate their spatial features with intrinsic and extrinsic effects. We find a high level of homogeneity, and show that polariton splitting variations are correlated with intrinsic exciton properties such as oscillator strength and linewidth. Moreover, we observe a deviation from thermal equilibrium in the resonant polariton population, which we ascribe to non-perturbative polariton-phonon coupling. Our measurements reveal a promisingly consistent polariton landscape, and highlight the importance of phonons for future polaritonic devices.

Exciton polaritons can enable novel photonic elements such as ultra-low threshold lasers [1, 2], Bose-Einstein condensates [3], or quantum nonlinear optical elements [4]. Atomically thin crystals of TMDs offer a particularly promising platform to study and harness exciton polaritons due to a strong exciton binding energy [5, 6] and a large oscillator strength [7–9]. Both properties in concert have enabled the demonstration of exciton polaritons at room temperature [10–12] and under cryogenic conditions [13–15]. Owing to their unique spin-valley degrees of freedom inherited from the non-centrosymmetric host crystal with strong spin-orbit effects [16], TMD polaritons could enable novel photonic devices with topological properties in accordingly structured two-dimensional photonic and excitonic landscapes [17].

It remains an important task to understand the conditions that govern polariton properties, and to realize large-scale systems that are useful also for such advanced devices. Elevated temperature and the crystals' two-dimensional geometry constitute an environment that strongly influences polariton properties. Variation of both intrinsic defect concentrations and of the dielectric surrounding can lead to a significant spatial variation of the materials optical properties, and phonons couple strongly to the optical transition. In this work we study such spatial variations and environmental influences by scanning cavity microscopy in the strong coupling regime. We reveal correlations with intrinsic excitonic properties and observe a polariton population with significant de-

viations from thermal equilibrium, indicative of a non-Markovian polariton-phonon coupling.

Our experimental platform is a fiber-based Fabry-Perot microcavity [18] consisting of a laser-machined optical fiber serving as a micromirror and a planar mirror with monolayer flakes of WS₂ synthesized by chemical vapor deposition (CVD) and covered with a thin film of PMMA (see Fig. 1a and Methods). Away from the flakes, the transmission of the bare cavity shown in Fig. 1b features the characteristics of a stable Fabry-Perot resonator with Hermite-Gaussian eigenmodes that exhibits a strong main resonance and a blue-detuned weak resonance stemming from higher transverse modes. The empty cavity has a finesse of 40 at the exciton energy of 2.01 eV, leading to a cavity-length dependent linewidth $\kappa = 51/q$ meV, where q is the longitudinal mode order.

In the first experimental step, we characterized the CVD-grown WS₂ monolayer flakes on the macroscopic mirror with confocal microscopy and spectroscopy and found extended triangular flakes with bright PL as in Fig. 1c. We observe PL spectra as shown in Fig. 1d with a full-width-half-maximum (FWHM) linewidth $\gamma = 33$ meV, typical for monolayer WS₂ [19]. For the same position, we also measured the absorption spectrum of Fig. 1c by cavity-enhanced spectroscopy at large mirror separation where the exciton-photon coupling is weak (see methods). The absorption spectrum matches the center energy and the linewidth of the emission, but shows additional finite background absorption at the higher energy side of the resonance.

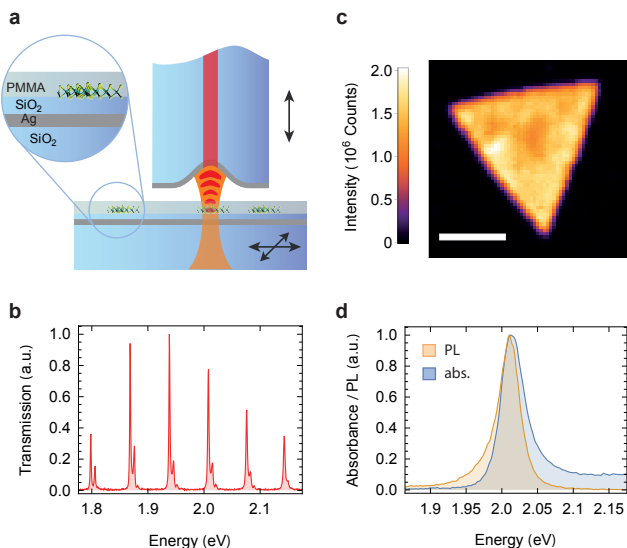


FIG. 1: **Experimental setup and characterisation.** a) A fiber-based microcavity couples to monolayer WS_2 covered with a thin film of PMMA on top of a silver (Ag) mirror capped with a dielectric spacer (SiO_2). The planar mirror is mounted on a 3D nanopositioning stage to enable raster-scanning of the sample through the cavity mode and coarse tuning of the mirror separation. The cavity length and thus its resonance frequency can be fine-tuned by a piezo actuator moving the fiber. b) White light transmission spectrum of the empty cavity for a large mirror separation $d = 10.5 \mu\text{m}$. c) Confocal photoluminescence map of a WS_2 flake on the mirror (scale bar $10 \mu\text{m}$). d) Confocal photoluminescence (orange) and cavity-assisted absorption (blue) spectra recorded on a typical position of a WS_2 flake on the mirror.

After these initial studies of confocal PL and absorption of monolayer WS_2 flakes at large cavity-mirror separation, we reduced the intermirror distance to increase the cavity-flake coupling. For a mirror separation corresponding to the cavity mode order $q = 4$, Fig. 2a shows the cavity transmission spectra on (blue) and off (orange) the flake under white light illumination. The WS_2 transmission spectrum exhibits a pronounced normal mode splitting with two well-resolved polariton resonances in response to the fundamental cavity mode, and a weak higher-energy resonances due to transverse modes of the cavity. Tuning the cavity resonance across the emission spectrum results in avoided level crossing with spectra in Fig. 2b, which we compare to a coupled oscillator model in Fig. 2c and d.

The model accounts for the coupling with strength g between an optical cavity with the fundamental mode decay rate κ_0 and an exciton transition with homogeneous linewidth γ to obtain the normal-mode or Rabi splitting Ω of the coupled oscillator system [20]:

$$\Omega(q) = 2\sqrt{\sqrt{g^4 + 2g^2\gamma(\gamma + \kappa_0/q)} - \gamma^2}. \quad (1)$$

To model the detuning-dependent dispersion of the upper and lower polariton modes shown in Fig. 2c we take $\kappa_0 = 51 \text{ meV}$ and $\gamma = 33 \text{ meV}$ as determined from the initial characterization described above and use g as the only free fit parameter. Figure 2e shows the observed splitting and the deduced light-matter coupling strength g as a function of the longitudinal mode order q .

The splitting is smaller than reported in a similar experiment [11] (with $\hbar\Omega \approx 50 \text{ meV}$ at $q = 4$), which can be traced back to a non-ideal PMMA layer thickness that reduces the local field at the sample in our experimental configuration. We note, however, that we use a stable microcavity where excitons couple to a single, spectrally isolated cavity mode, while in [11] a planar Fabry-Perot displaying a mode continuum was used.

The model also accounts for the detuning dependence of the upper and lower polariton branch linewidths with $\Gamma = (\kappa + \gamma)/2$ on resonance (Fig. 2d). Since the cavity linewidth κ is significantly narrower than the exciton linewidth γ , coupling leads to a reduced polariton linewidth and thus to an increase of the polariton lifetime compared to the exciton lifetime by a factor of 1.7 on resonance, and up to a factor 4 at large detuning.

The observations of normal mode splitting and line narrowing as hallmarks of the strong-coupling regime are robust characteristics of the light-matter coupling for our sample. The right panel of Fig. 2f shows cavity-enhanced absorption measurements of other individual triangular WS_2 monolayers. The left panel of Fig. 2f shows the statistics of resonant coupling experiments at $q = 4$ carried out on 14 of such flakes: while 10 flakes exhibited splitting energies in the range of $\hbar\Omega = 22 - 36 \text{ meV}$, four flakes did not exhibit signatures of strong coupling at all. Remarkably, most WS_2 flakes in strong coupling featured comparable coupling strengths with a variation in g of only $\pm 3 \text{ meV}$.

Having established the signatures of strong coupling at individual spatial positions, we utilized the scanning capabilities of our cavity [21, 22] to study the two-dimensional nature of polariton landscapes in extended WS_2 flakes. To this end, we stabilized the cavity length at $q = 4$ and ensure symmetric polariton populations as monitored in transmission spectroscopy. Under such conditions, the sample was displaced with respect to the cavity mode in $1 \mu\text{m}$ steps corresponding to the spatial resolution determined by the cavity mode waist. At each raster-scan pixel we recorded white-light transmission spectra of the cavity as in Fig. 3a to infer the polariton splitting, shown in Fig. 3b, and the center energy of the polariton doublet, shown in Fig. 3c.

First, we accounted for the spatial overlap between the cavity mode and the flake. Figure 3d shows how the observed Rabi splitting scales with the area overlap η . The dependence agrees very well with the expectation for collective coupling, where $g \sim \sqrt{\eta}$. To eliminate this overlap effect from further analysis, the map of Fig. 3b was cor-

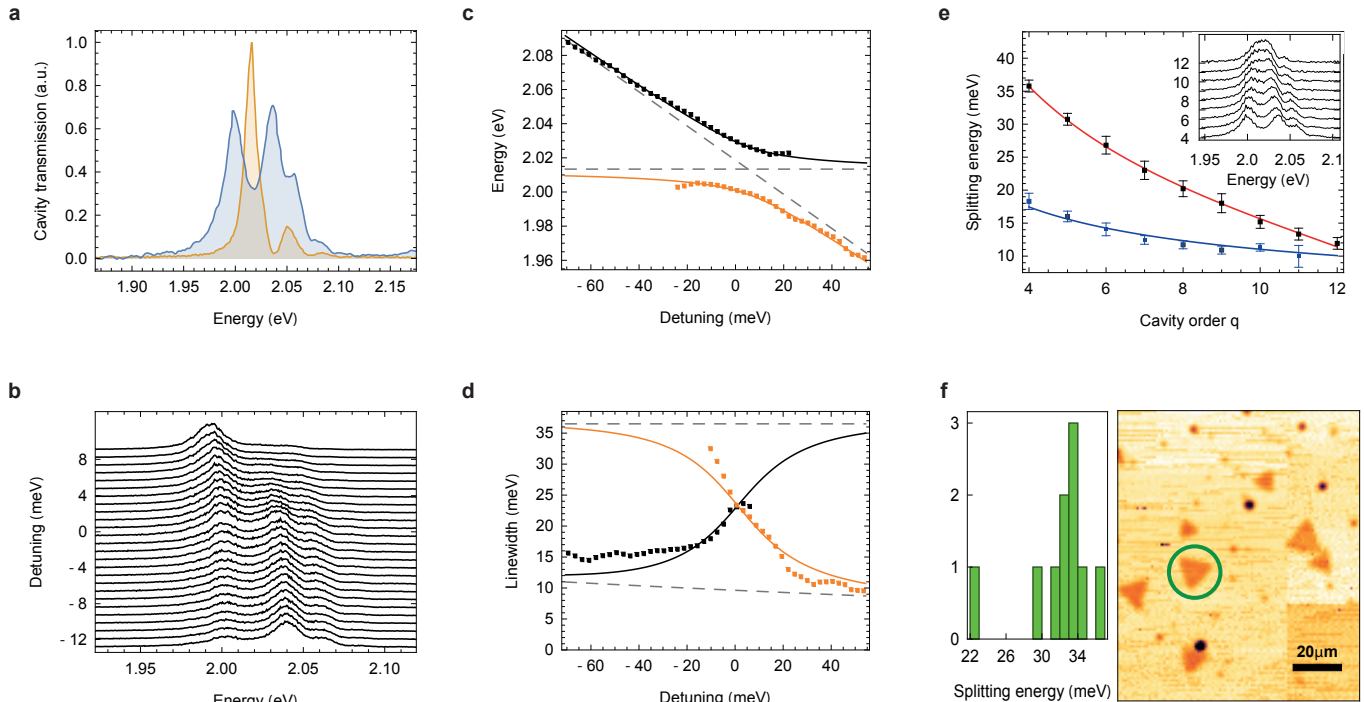


FIG. 2: **Polariton spectroscopy.** (a) Bare cavity transmission spectrum (orange) and transmission spectrum under normal mode splitting at mode order $q = 4$ (blue). (b) Cavity transmission spectra of the $q = 4$ mode when tuned stepwise across the exciton resonance by varying the mirror separation. (c) Resonance energies of the upper (black) and lower (orange) polariton branches (data) derived from the spectra in b) and fits to the coupled oscillator model (solid lines; dashed lines show the empty cavity and bare exciton resonances). (d) Extracted linewidths of the upper (black) and lower (orange) polariton branches (data) and model fits (solid lines; the upper and lower dashed lines show the linewidths of the empty cavity and the bare exciton resonances, respectively). (e) Polariton splitting $\hbar\Omega$ (upper data, fitted red line, see text) and coupling strength g (lower data and blue line) as a function of cavity mode order q evaluated from the spectra shown in the inset. (f) Statistics of polariton splitting observed for 10 different flakes (left) and a map of cavity-enhanced sample extinction (right).

rected to show actual Rabi splitting values renormalized as $\Omega = \Omega_{raw}/\sqrt{\eta}$. Similar overlap corrections were performed for the photoluminescence and absorption map Fig. 3 f, j, according to $1/\eta$, and all data shown is limited to $\eta > 0.35$. The remaining deviations at edges are consistent with the notion of edges as line defects with light-matter characteristics distinct from the flake interior [23].

It is instructive to confront the maps of polariton characteristics in the top panel of Fig. 3 with complementary parameters of light-matter coupling probed for the same flake with resonant absorption (central panel of Fig. 3) and PL (bottom panel of Fig. 3). The absorption spectrum of Fig. 3e was recorded for a large mirror separation ($\sim 10 \mu\text{m}$) and used to evaluate the peak absorption (Fig. 3f) and its center energy (Fig. 3g). For similar conditions, we also record the PL spectrum (Fig. 3i) and extracted the peak PL (Fig. 3j) and linewidth (Fig. 3k).

This comprehensive set of spatially-resolved measurements allows us to correlate external and internal properties of light-matter interaction in monolayer WS_2 . The

polariton splitting in Fig. 3b shows a high degree of homogeneity with moderate variation across the flake, and a localized maximum along a line parallel to the left edge. This region is also apparent in a blue-shift of the polariton center energy E_{cp} (Fig. 3c) and also in the absorption center energy E_c (Fig. 3g). The transition energy is sensitive to various internal and external parameters including strain [24–26], doping [27], or screening due to the dielectric environment [28–31].

Based on our data, strain is an unlikely explanation since it would correlate with the PL yield. However, we do not observe significant correlations between PL and E_c . We also find no indication of a doping-induced energy shift, since no trion contribution was observed in the spectra [32]. The most probable scenario is that variations in the local dielectric environment are responsible for the inhomogeneities in light-matter coupling across the flake. The process used to transfer the flakes onto the mirror can lead to adsorbates such as water or KOH molecules located between the WS_2 flake and the SiO_2 surface, thereby introducing variations in the distance

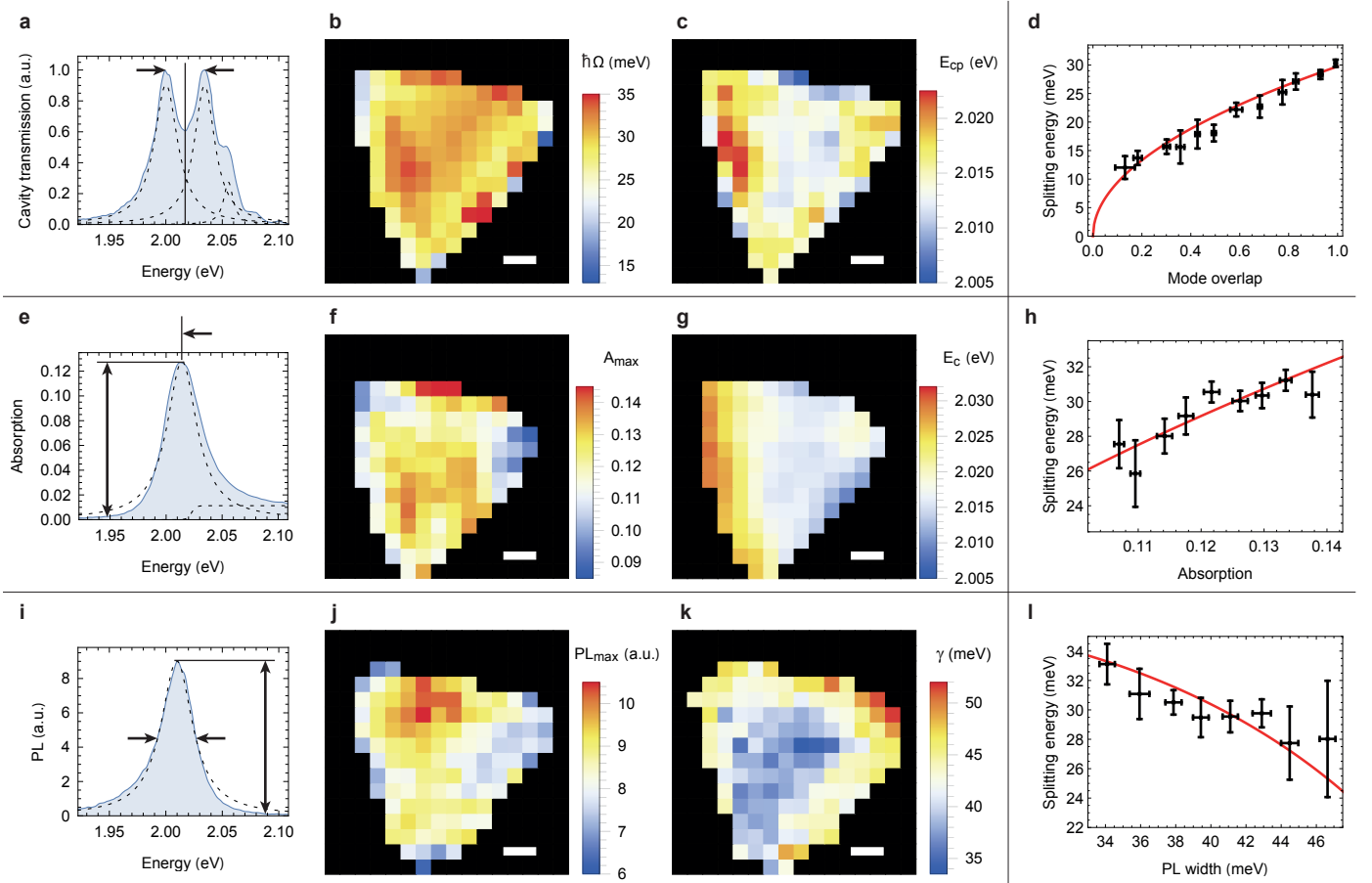


FIG. 3: **Polariton hyperspectral imaging.** a) Resonant cavity transmission showing a normal mode spectrum at $q = 4$. Spatial maps of b) the Rabi splitting energy $\hbar\Omega$, and c) the center energy of the normal mode spectrum E_{cp} . d) Dependence of $\hbar\Omega$ on the spatial mode overlap with the flake. e) Absorption spectrum at large q as inferred from white light transmission spectroscopy. Maps of f) the maximal resonant absorption A_{max} , and g) of the absorption center energy E_c . h) Correlation between $\hbar\Omega$ and the maximum resonant absorption, together with a fit (solid line, see text). i) Photoluminescence spectrum, j) map of the peak photoluminescence intensity, and k) photoluminescence linewidth. l) Correlation between $\hbar\Omega$ and the photoluminescence linewidth together with a fit to Eq. 1 (solid line). The scale bar shows $2 \mu\text{m}$ in all maps.

between the WS_2 monolayer and the substrate. It is well known that the dielectric environment has an extraordinarily large impact on the excitonic properties of semiconductor monolayers, causing line shifts of up to hundreds of meV [28–31]. Our calculations show that variations of about 1 nm in the interlayer distance result in an energy shift of ~ 10 meV, consistent with our experimental observations (see Supplementary Information).

Comparing the splitting $\hbar\Omega$ with the resonant absorption map A_{max} shows a clear linear correlation, see Fig. 3h. Indeed this follows the expectation for an exciton oscillator strength that is directly proportional to the absorption, evidencing that the observed variations in A_{max} are dominated by radiative excitonic transitions rather than quenching induced by defects. Notably, there is no apparent correlation between the integrated PL and the splitting. However, a clear correlation can be ob-

served for the PL linewidth (and similarly for the absorption linewidth, not shown). As expected from Eq. 1, an anti-correlation between Ω and γ is expected. Originating either in excessive pure dephasing or inhomogeneous broadening, the increased linewidth towards the edges of the flake indicate an increased inhomogeneity and dissipation at these locations. Figure 3l shows good agreement between the observed linewidth dependence of the Rabi splitting and Eq. 1. Since the PL linewidth and the absorption center energy remain rather constant in the area where the absorption displays its largest variation, the different dependencies can be disentangled to a high degree, and the correlations shown in Fig. 3h,l) are dominated by a single quantity. Overall, we find that the variation in polariton splitting is governed by spatial variation of resonant absorption, inhomogeneous broadening and excessive pure dephasing or dissipation. With this we can link the polariton splitting to intrinsic exciton

properties in a quantitative way.

Finally, we turn to the influence of phonons on the polariton spectrum. It was suggested that phonons can lead to a surprising departure from a semi-classical description of the polaritons [33, 34]. The directly observable effect is that the phonon bath mediates direct transitions between the dressed states and thereby affects the polariton population. In the experiment, we inspect the polariton population for exact cavity resonance conditions, i.e. where the polariton splitting is minimal for a given mode order q . Figure 4a shows the spectra for different q . A large asymmetry is apparent, which increases non-monotonically for decreasing cavity mode order. We do not expect other processes such as exciton-electron scattering or exciton-exciton scattering to be relevant for our experimental conditions since we observe no signs of trions and excite with sufficiently low powers such that the exciton population remains small. We evaluate the population ratio p_u/p_l of the upper and lower polariton resonance from fits to the spectra and display the result as a function of the polariton splitting energy, see Fig. 4c. In this way, we can perform spectroscopy of the inter-polariton scattering strength within a single device at a fixed temperature. This is advantageous since the sample properties and the phonon bath remain fixed in this way. We find that the overall behavior is consistent with a thermal occupation following a Boltzmann distribution [35] $p_u/p_l = \exp -\hbar\Omega/k_B T$ (solid line in Fig. 4b, no free parameters), but with a significant deviation in particular for mode order $q = 7$ ($\hbar\Omega = 23\text{meV}$) and $q = 9$ ($\hbar\Omega = 18\text{meV}$), where the upper polariton remains significantly more populated than for a thermalized distribution.

Such a deviation could originate from a phonon bottleneck, resulting from a low phonon density of states at the relevant energy, such that thermalization is suppressed. However, the splitting energy of mode $q = 7$ ($q = 9$) coincides with the energy of longitudinal acoustic (transverse acoustic) phonons at the K point with a significant density of states [36]. Indeed it has been shown that a large exciton-phonon coupling strength is present under resonant conditions by exciton luminescence up-conversion [37]. The apparent impact of K-point phonons here suggests that transitions between polaritons states are accompanied by inter-valley scattering. The resonant polariton-phonon coupling establishes a non-thermal distribution indicative of non-Markovian dynamics [34, 35, 38]. Such a scenario is expected to lead to superposition states involving polariton, valley, and phonon degrees of freedom [34] with emergent quantum correlations [33].

Our work shows that spatial variations in the optical properties of atomically thin semiconductors and their local environment influence the polariton states of a coupled monolayer-microcavity system and lead to variations in the polariton splitting on a few-micron scale within a

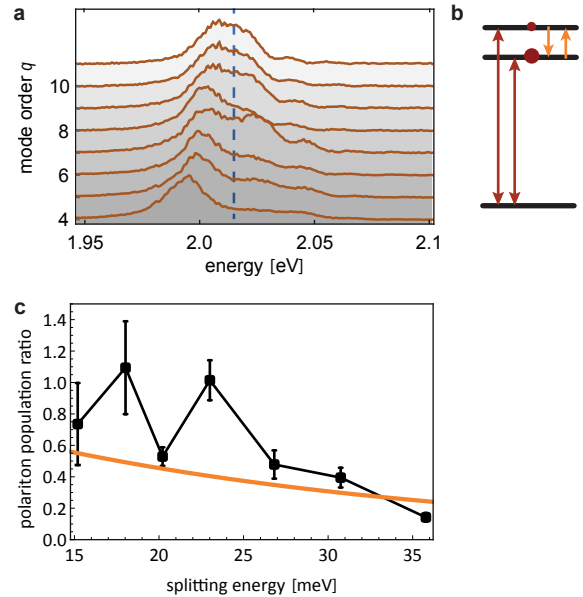


FIG. 4: **Polariton asymmetry due to phonon transitions.** a) Normal mode spectra for different mode orders $q = 4 - 11$ with the cavity tuned to exact resonance with the exciton. b) Schematic level scheme of the ground state and two polariton states with optical (red) and phonon (orange) transitions. c) Polariton population ratio as a function of polariton splitting energy. The solid line shows the Boltzmann distribution.

flake, as well as for different flakes. Clear correlations were established interconnecting local variations in the oscillator strength and the exciton linewidth with the Rabi splitting. While the observed variations are already encouragingly small, further improvement in homogeneity is expected for flakes embedded in van der Waals heterostructures e.g. with hexagonal boron nitride. This could open the way for advanced polaritonic devices such as tunable polariton lasers and polariton Bose-Einstein condensation, and enable the realization of topological polaritons [17]. Furthermore, the resonant interaction of polaritons with phonons leads to a significant alteration of the polariton population, with marked deviations from a thermal distribution. While further studies are required to elucidate this behavior, the observed strong polariton-phonon coupling could provide a novel resource for polaritonic devices.

Methods

Cavity characterization

The mirrors were prepared by evaporating 50 nm silver as reflective layer and a 20 nm (100 nm) SiO_2 capping layer on top which protects silver from oxidation and serves as a spacer layer to place the sample at a field

antinode. The fiber, shaped by CO₂ laser machining [39], has a conical tip to achieve smallest mirror separations [40]. In its center, we fabricate a concave profile with a radius of curvature of 75 μm and a depth of 200 nm. We measure the cavity finesse \mathcal{F} with a laser at 532 nm and obtain a value $\mathcal{F} = 30$, and $\mathcal{F} = 40$ from white light transmission spectra at the exciton emission energy $E_0 = 2.01$ eV, in good agreement with a simulation. To calibrate the optical cavity length, we record broad-band cavity transmission spectra with a supercontinuum laser and evaluate the separation of subsequent cavity resonances, see Fig. 1b. We find that the smallest accessible effective cavity length is $d_{\text{eff}} = 4\lambda/2$, corresponding to the longitudinal mode order $q = 4$, limited by the profile depth (200 nm) and the presence of the PMMA layer which covers the sample. At this separation, we obtain a cavity quality factor of $Q_c = q\mathcal{F} = 200$. From scanning-cavity microscopy measurements and calculations, we infer the mode waist to be $w_0 = 1.0$ μm , which approximately defines the spatial resolution of the scanning cavity microscope.

Sample preparation

WS₂ monolayer crystals were grown by sulfurization of tungsten dioxide (WO₂) powder. A SiO₂/Si substrate along with a WO₂ powder boat were placed at the center of a chemical vapor deposition (CVD) furnace. The SiO₂/Si substrate was facing down in close proximity to the WO₂ powder (99.99%, Sigma Aldrich). The temperature was initially ramped up rapidly but slowed down to 3°C /min as it approached to 850°C. Sulfur powder (99.5%, Alfa Aesar) was placed at upstream end of the quartz tube in a separate boat near the heating zone to allow vaporization ($\sim 110^\circ\text{C}$) during the growth. The growth temperature was maintained for 15 minutes before cooling it down to the room temperature. 200 SCCM of Argon was used as a carrier gas during the entire process. As-grown monolayer crystals were studied in spectroscopy or transferred onto a mirror using established polymer-supported wet method. To this end polymethyl methacrylate (PMMA) was spin-coated on the monolayer flakes and lifted off in 1M potassium hydroxide (KOH) in water. The PMMA-supported film with WS₂ crystal flakes was rinsed in water for three cycles at room temperature to remove possible KOH residue and finally transferred onto mirror substrates.

Photoluminescence microscopy and spectroscopy

Excitation was performed either with a cw laser at 532nm for PL or with a pulsed supercontinuum (Fianium Whitelase 450 SC, 20 MHz, ~ 50 ps) filtered to a spectral band of 580 nm to 650 nm. Confocal measurements

were performed in a homebuilt setup including a 0.9 NA air objective. Detection was performed either with a Si avalanche photodetector or with a grating spectrometer (Princeton Instruments, Acton 2500) equipped with a sensitive CCD camera (Andor ikon-M). To observe the polariton spectrum we perform broad-band transmission spectroscopy of the coupled cavity-emitter system. We reduce the laser power such that during the pulse, much less than one photon populates the cavity on average to avoid multi-photon processes. The transmitted light was spectrally filtered, fiber coupled and recorded with the grating spectrometer.

Model for environmental exciton energy renormalization

To assess the impact of variations in the distance between the optically active WS₂ flake and the SiO₂ substrate, we employ a multiscale approach introduced in Ref. [31]. In a first step, an electrostatic model is used to determine an effective non-local dielectric function to account for screening of Coulomb interaction between carriers in the TMD in a vertical heterostructure environment. In a second step, band-structure renormalizations and the screened Coulomb potential enter calculations of the optical properties to determine the spectral positions of the excitonic resonances.

Acknowledgments

We thank Thomas Hümmer, Julia Benedikter, Matthias Mader and Hanno Kaupp for support. Fruitful discussions with Jonathan Finley and Michael Kaniber are acknowledged. The work has been funded by the DFG Cluster of Excellence NIM, the Volkswagen Foundation, and the European Research Council (ERC) under the ERC grant agreement no. 336749. T. W. Hänsch acknowledges funding from the Max-Planck Foundation.

Author contributions

D.H. and A.H. conceived the project, C.G. and M.F. designed and set up the experiment, H.Y., I.B. and A. D. M. prepared the sample, C.G. and M.F. collected the data, C.G., A.H., C. Gies, M. Florian, M.H., and D.H. analyzed and modeled the data. C.G., A.H. and D.H. wrote the manuscript. All authors contributed to the discussion of the results and the manuscript.

* To whom correspondence should be addressed. E-mail: david.hunger@kit.edu

- [1] Fraser, M. D., Höfling, S. & Yamamoto, Y. Physics and applications of exciton-polariton lasers. *Nature Materials* **15**, 1049 (2016).
- [2] Ye, Y. *et al.* Monolayer excitonic laser. *Nature Photonics* **9**, 733 (2015).
- [3] Jiang, J.-H. & John, S. Photonic architectures for equilibrium high-temperature bose-einstein condensation in dichalcogenide monolayers. *Scientific Reports* **4**, 7432 (2014).
- [4] Verger, A., Ciuti, C. & Carusotto, I. Polariton quantum blockade in a photonic dot. *Phys. Rev. B* **73**, 193306 (2006).
- [5] Ramasubramaniam, A. Large excitonic effects in monolayers of molybdenum and tungsten dichalcogenides. *Phys. Rev. B* **86**, 115409 (2012).
- [6] Chernikov, A. *et al.* Exciton binding energy and nonhydrogenic Rydberg series in monolayer WS₂. *Phys. Rev. Lett.* **113**, 076802 (2014).
- [7] Mak, K. F., Lee, C., Hone, J., Shan, J. & Heinz, T. F. Atomically thin MoS₂: A new direct-gap semiconductor. *Phys. Rev. Lett.* **105**, 136805 (2010).
- [8] Splendiani, A. *et al.* Emerging photoluminescence in monolayer mos₂. *Nano Letters* **10**, 1271–1275 (2010).
- [9] Li, Y. *et al.* Measurement of the optical dielectric function of monolayer transition-metal dichalcogenides: mos₂, MoSe₂, ws₂, and WSe₂. *Phys. Rev. B* **90**, 205422 (2014).
- [10] Liu, X. *et al.* Strong light-matter coupling in two-dimensional atomic crystals. *Nature Photonics* **9**, 30 (2015).
- [11] He, L. C. F. Z. *et al.* Room-temperature exciton-polaritons with two-dimensional WS₂. *Scientific Reports* **6**, 33134 (2016).
- [12] Lundt, N. *et al.* Room-temperature tamm-plasmon exciton-polaritons with a WSe₂ monolayer. *Nature Communications* **7**, 13328 (2016).
- [13] Dufferwiel, S. *et al.* Exciton-polaritons in van der Waals heterostructures embedded in tunable microcavities. *Nature Communications* **6**, 8579 (2015).
- [14] Wang, Q. *et al.* Direct observation of strong light-exciton coupling in thin WS₂ flakes. *Opt. Express* **24**, 7151 (2016).
- [15] Sidler, M. *et al.* Fermi polaron-polaritons in charge-tunable atomically thin semiconductors. *Nature Physics* **13**, 255 (2017).
- [16] Xiao, D., Liu, G.-B., Feng, W., Xu, X. & Yao, W. Coupled spin and valley physics in monolayers of MoS₂ and other group-IV dichalcogenides. *Phys. Rev. Lett.* **108**, 196802 (2012).
- [17] Karzig, T., Bardyn, C.-E., Lindner, N. H. & Refael, G. Topological polaritons. *Physical Review X* **5**, 031001 (2015).
- [18] Hunger, D. *et al.* Fiber Fabry-Perot cavity with high finesse. *New J. Phys.* **12**, 065038 (2010).
- [19] Molas, M. R. *et al.* The optical response of monolayer, few-layer and bulk tungsten disulfide. *Nanoscale* **9**, 13128–13141 (2017).
- [20] Savona, V., Andreani, L. C., Schwendimann, P. & Quattropani, A. Quantum well excitons in semiconductor microcavities: Unified treatment of weak and strong coupling regimes. *Solid State Communications* **93**, 733–739 (1995).
- [21] Mader, M., Reichel, J., Hänsch, T. W. & Hunger, D. A scanning cavity microscope. *Nature Communications* **6**, 7249 (2015).
- [22] Hümmer, T. *et al.* Cavity-enhanced raman microscopy of individual carbon nanotubes. *Nature Communications* **7**, 12155 (2016).
- [23] Neumann, A. *et al.* Opto-valleytronic imaging of atomically thin semiconductors. *Nature Nanotechnol.* **12**, 329–334 (2017).
- [24] Conley, H. J. *et al.* Bandgap engineering of strained monolayer and bilayer MoS₂. *Nano Letters* **13**, 3626 (2013).
- [25] Steinhoff, A. *et al.* Efficient excitonic photoluminescence in direct and indirect band gap monolayer MoS₂. *Nano Letters* **15**, 6841 (2015).
- [26] He, X. *et al.* Strain engineering in monolayer WS₂, MoS₂ and the WS₂/MoS₂ heterostructure. *Appl. Phys. Lett.* **109**, 173105 (2016).
- [27] Chernikov, A. *et al.* Electrical tuning of exciton binding energies in monolayer WS₂. *Phys. Rev. Lett.* **115**, 126802 (2015).
- [28] Ugeda, M. M. *et al.* Giant bandgap renormalization and excitonic effects in a monolayer transition metal dichalcogenide semiconductor. *Nature Materials* **13**, 1091 (2014).
- [29] Rösner, M. *et al.* Two-dimensional heterojunctions from nonlocal manipulations of the interactions. *Nano Lett.* **16**, 2322 (2016).
- [30] Raja, A. *et al.* Coulomb engineering of the bandgap and excitons in two-dimensional materials. *Nature Commun.* **8**, 15251 (2017).
- [31] Florian, M. *et al.* The dielectric impact of layer distances on exciton and trion binding energies in van der Waals heterostructures. *arXiv:1712.05607* (2017).
- [32] Plechinger, G. *et al.* Identification of excitons, trions and biexcitons in single-layer WS₂. *Phys. Status Solidi RRL* **9**, 4547–461 (2015).
- [33] Iles-Smith, J. & Nazir, A. Quantum correlations of light and matter through environmental transitions. *Optica* **3**, 207 (2016).
- [34] Chovan, J., Perakis, I. E., Ceccarelli, S. & Lidzey, D. G. Controlling the interactions between polaritons and molecular vibrations in strongly coupled organic semiconductor microcavities. *Phys. Rev. B* **78**, 045320 (2008).
- [35] Michetti, P. & La Rocca, G. C. Exciton-phonon scattering and photoexcitation dynamics in J-aggregate microcavities. *Phys. Rev. B* **79**, 035325 (2009).
- [36] Molina Sanchez, A. & Wirtz, L. Phonons in single-layer and few-layer MoS₂ and WS₂. *Phys. Rev. B* **84**, 155413 (2011).
- [37] Jones, A. M. *et al.* Excitonic luminescence upconversion in a two-dimensional semiconductor. *Nature Physics* **12**, 323 (2015).
- [38] Liberato, S. D. & Ciuti, C. Stimulated scattering and lasing of intersubband cavity polaritons. *Phys. Rev. Lett.* **102**, 136403 (2009).
- [39] Hunger, D., Deutsch, C., Barbour, R. J., Warburton, R. J. & Reichel, J. Laser micro-fabrication of concave, low-roughness features in silica. *AIP Advances* **2**, 012119 (2012).
- [40] Kaupp, H. *et al.* Purcell-enhanced single-photon emission from nitrogen-vacancy centers coupled to a tunable microcavity. *Phys. Rev. Applied* **6**, 054010 (2016).

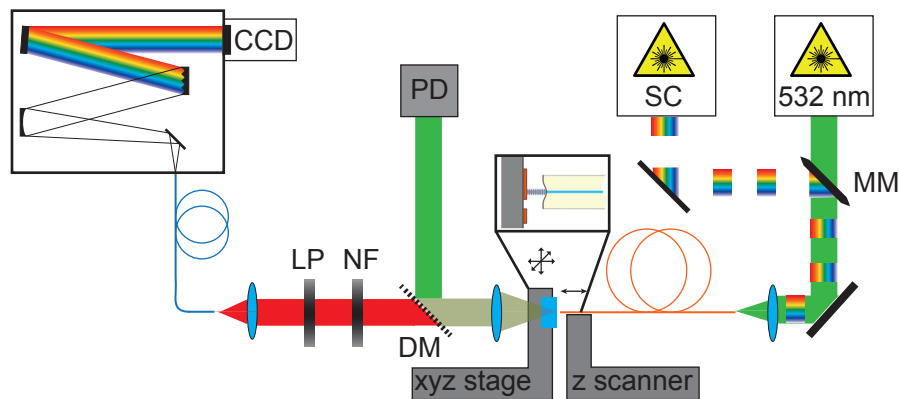


FIG. 5: Schematic drawing of the setup.

SUPPLEMENTARY INFORMATION

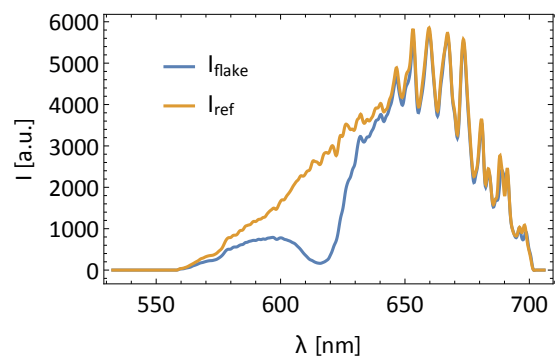
SETUP

Two laser sources can be coupled into the cavity fiber: a pulsed super-continuum source (SC) and a 532nm cw laser which can be selected via a motorized mirror (MM). The fiber can be moved in z-direction with sub-nm precision via a piezo actuator, while the sample is mounted on an attocube nanopositioner (ECS3030) with three translational degrees of freedom. The collected light is split into two paths with a dichroic mirror (DM). The short wavelength part is detected with a photodiode (PD), the long wavelengths pass a notch filter (NF) and a longpass filter (LP) to be detected with a spectrometer consisting of different gratings and a CCD camera.

EVALUATION OF CAVITY TRANSMISSION SPECTRA

Cavity-enhanced absorption spectroscopy

We probe the transmission of broadband light from the SC source through the cavity with the grating spectrometer. We tune a set of cavity resonances stepwise across the spectrum and evaluate the resonances' peak transmission of multiple exposures to obtain a continuous spectrum. We perform measurements with a WS₂ flake located in the cavity mode (I_{flk}) and for an empty cavity as a reference (I_{ref}). We normalize the transmission spectrum to obtain the cavity-enhanced loss, $B_{\text{max}} = 1 - I_{\text{flk}}/I_{\text{ref}}$, and calculate the peak absorption A_{max} from B_{max} and the mirror reflectivity R as obtained from empty cavity measurements by solving the Fabry-

FIG. 6: Broadband cavity-enhanced transmission spectra taken for an empty cavity (orange) and with a WS₂ flake (blue).

Perot transmission function for A_{max} ,

$$A_{\text{max}} = \frac{2B_{\text{max}}(R(1-R) + (1-R^2))}{2R^2(1-B_{\text{max}})} + \frac{\sqrt{(1-R^2)^2 - 4B_{\text{max}}R(1-R)^2}}{2R^2(1-B_{\text{max}})}.$$

This yields calibrated absorption spectra as shown in the manuscript.

Fitting of transmission spectra

We fit all spectra showing normal mode splitting with a triple Lorentzian, accounting for the two polariton resonances and one additional higher order transverse mode of the cavity associated with the upper polariton. The transversal mode of the lower polariton is neglected in the analysis, since its peak is not resolvable in the spectrum, as it is the case for other higher order modes. We expect an analogous anti-crossing behavior of the transversal mode as for the fundamental mode. From this we

estimate that the transversal mode of the lower polariton contains less than 1% of the ground mode polariton intensities. We fit the following expression to the measured spectra:

$$S(\lambda) = a_{up} \frac{\Delta_{up}^2}{(\lambda - \lambda_{up})^2 - \Delta_{up}^2} + a_{lp} \frac{\Delta_{lp}^2}{(\lambda - \lambda_{lp})^2 - \Delta_{lp}^2} + a_{tm} \frac{\Delta_{tm}^2}{(\lambda - \lambda_{tm})^2 - \Delta_{tm}^2}$$

From the fits we extract the polariton wavelenghts $\lambda_{up}, \lambda_{lp}$, the full-widths at half maximum of the polariton branches Δ_{up}, Δ_{lp} , and the amplitudes a_{up}, a_{lp} . Care is taken to obtain optimal fitting, and only reasonable fit values are used for later evaluations.

Polariton dispersion

The complex polariton eigenfrequencies are given by the following expression [20]:

$$\omega = \frac{\omega_{ex} + \omega_c}{2} - i \frac{\gamma + \kappa}{4} \pm \sqrt{g^2 + \frac{1}{4} \left(\omega_{ex} - \omega_c - i \frac{\gamma - \kappa}{2} \right)^2}$$

The dispersion of the polaritons is given by the real part of the spectrum $Re(\omega)$. A simultaneous fit of the two branches to the dispersion data is performed to extract the coupling constant g and other parameters. We perform several fits and fix different parameters ((i) exciton and cavity linewidth, (ii) exciton energy and exciton and cavity linewidth, (iii) energy of zero detuning, exciton and cavity linewidth) in each case to obtain an estimate for the uncertainty of the fit.

Polariton width

The polariton linewidths are given by the imaginary part of the spectrum $-Im(\omega)$. A simultaneous fit of the linewidths to the two branches is performed to define the exciton linewidth γ . As for the dispersion relation, different parameters are fixed ((i) cavity linewidth, (ii) exciton energy and cavity linewidth, (iii) energy of zero detuning and cavity linewidth) to check the robustness of the fits. From the models, we obtain an exciton linewidth of $\gamma \approx 37$ meV, in good agreement with confocal measurements and from cavity-enhanced fluorescence spectroscopy at large mirror separation.

Polariton intensity

We account for the wavelength dependence of the SC source and of the background absorption of the sample when evaluating the polariton intensities. Therefore, the transmission spectra are normalized by the SC spectrum as measured after the cavity without a sample to include wavelength dependent coupling efficiencies (see section above on cavity-enhanced absorption spectroscopy). In a second step, the effect of background absorption is corrected by normalizing with the wavelength dependent intracavity loss (not including the resonant absorption from the exciton). The normalized polariton intensities are then fitted with

$$p_{u,l} = \Theta(\mp\delta) \cos \left[\frac{1}{2} \arctan \left(2 \frac{g}{\delta} \right) \right]^2 + \Theta(\pm\delta) \sin \left[\frac{1}{2} \arctan \left(2 \frac{g}{\delta} \right) \right]^2$$

for the upper and lower polaritons.

THEORETICAL MODEL OF DIELECTRIC SCREENING

In Fig.7, we quantify the effect that local variations in the interlayer distance can have on the optical properties of a WS₂ monolayer between a PMMA layer and a silicon oxide substrate. Shown is the dependence on the distance between the TMD and the SiO₂ substrate, while the distance between PMMA and TMD is fixed at a realistic value of 5 Å [1]. The top panel shows the dependence of the band gap at the K point and the exciton binding energy. The resulting impact on the spectral position of the A-exciton transition is shown in the bottom panel. A variation of the gap to silicon oxide between 0.4 nm and 1.4 nm leads to a shift of the excitonic absorption peak of about 11 meV, which agrees with the variation observed in Fig. 3g in the main text.

* To whom correspondence should be addressed. E-mail: david.hunger@kit.edu

[1] Rooney, A. P. *et al.* Observing imperfection in atomic interfaces for van der waals heterostructures. *Nano Lett.* **17**, 5222 (2017).

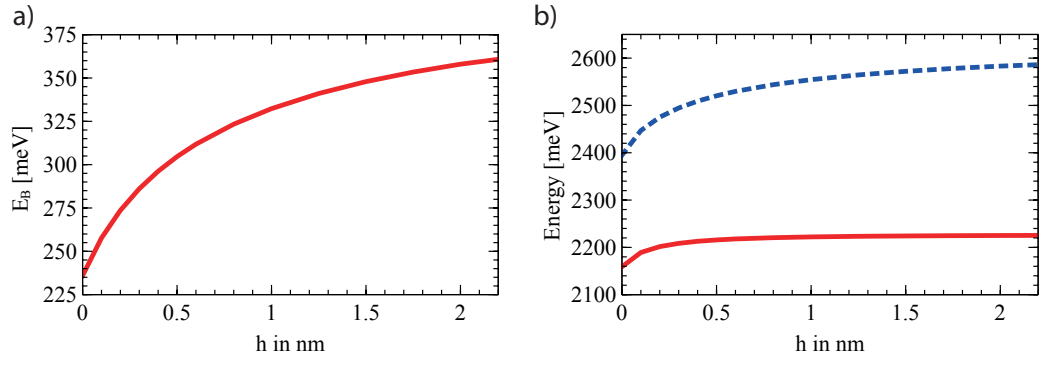


FIG. 7: a) Exciton binding energy as a function of the distance h between the WS₂ flake and the SiO₂ substrate. b) Resulting gap-dependent center energy of the excitonic absorption peak (red line) and electronic band gap (blue dotted line).